

University of Groningen

Focused helium and neon ion beam induced etching for advanced extreme ultraviolet lithography mask repair

Gonzalez, Carlos M.; Timilsina, Rajendra; Li, Guoliang; Duscher, Gerd; Rack, Philip D.; Slingenbergh, Winand; van Dorp, Willem F.; De Hosson, Jeff T. M.; Klein, Kate L.; Wu, Huimeng M.

Published in:
Journal of Vacuum Science & Technology B

DOI:
[10.1116/1.4868027](https://doi.org/10.1116/1.4868027)

IMPORTANT NOTE: You are advised to consult the publisher's version (publisher's PDF) if you wish to cite from it. Please check the document version below.

Document Version
Publisher's PDF, also known as Version of record

Publication date:
2014

[Link to publication in University of Groningen/UMCG research database](#)

Citation for published version (APA):

Gonzalez, C. M., Timilsina, R., Li, G., Duscher, G., Rack, P. D., Slingenbergh, W., ... Stern, L. A. (2014). Focused helium and neon ion beam induced etching for advanced extreme ultraviolet lithography mask repair. *Journal of Vacuum Science & Technology B*, 32(2), [021602]. <https://doi.org/10.1116/1.4868027>

Copyright

Other than for strictly personal use, it is not permitted to download or to forward/distribute the text or part of it without the consent of the author(s) and/or copyright holder(s), unless the work is under an open content license (like Creative Commons).

Take-down policy

If you believe that this document breaches copyright please contact us providing details, and we will remove access to the work immediately and investigate your claim.

Downloaded from the University of Groningen/UMCG research database (Pure): <http://www.rug.nl/research/portal>. For technical reasons the number of authors shown on this cover page is limited to 10 maximum.

Focused helium and neon ion beam induced etching for advanced extreme ultraviolet lithography mask repair

Carlos M. Gonzalez, Rajendra Timilsina, Guoliang Li, Gerd Duscher, Philip D. Rack, Winand Slingenberg, Willem F. van Dorp, Jeff T. M. De Hosson, Kate L. Klein, Huimeng M. Wu, and Lewis A. Stern

Citation: *Journal of Vacuum Science & Technology B* **32**, 021602 (2014); doi: 10.1116/1.4868027

View online: <https://doi.org/10.1116/1.4868027>

View Table of Contents: <http://avs.scitation.org/toc/jvb/32/2>

Published by the [American Vacuum Society](#)

Articles you may be interested in

[Review Article: Advanced nanoscale patterning and material synthesis with gas field helium and neon ion beams](#)

Journal of Vacuum Science & Technology B, Nanotechnology and Microelectronics: Materials, Processing, Measurement, and Phenomena **35**, 030802 (2017); 10.1116/1.4981016

[Helium ion microscopy](#)

Journal of Vacuum Science & Technology B, Nanotechnology and Microelectronics: Materials, Processing, Measurement, and Phenomena **32**, 020801 (2014); 10.1116/1.4863676

[Gas field ion source and liquid metal ion source charged particle material interaction study for semiconductor nanomachining applications](#)

Journal of Vacuum Science & Technology B, Nanotechnology and Microelectronics: Materials, Processing, Measurement, and Phenomena **28**, C6F15 (2010); 10.1116/1.3511509

[Nanomachining with a focused neon beam: A preliminary investigation for semiconductor circuit editing and failure analysis](#)

Journal of Vacuum Science & Technology B, Nanotechnology and Microelectronics: Materials, Processing, Measurement, and Phenomena **29**, 06F604 (2011); 10.1116/1.3660797

[Gas-assisted focused electron beam and ion beam processing and fabrication](#)

Journal of Vacuum Science & Technology B: Microelectronics and Nanometer Structures Processing, Measurement, and Phenomena **26**, 1197 (2008); 10.1116/1.2955728

[Sub-10-nm nanolithography with a scanning helium beam](#)

Journal of Vacuum Science & Technology B: Microelectronics and Nanometer Structures Processing, Measurement, and Phenomena **27**, L18 (2009); 10.1116/1.3182742



Instruments for Advanced Science


Contact Hiden Analytical for further details:
W www.HidenAnalytical.com
E info@hiden.co.uk

[CLICK TO VIEW](#) our product catalogue




Gas Analysis

- dynamic measurement of reaction gas streams
- catalysis and thermal analysis
- molecular beam studies
- dissolved species probes
- fermentation, environmental and ecological studies




Surface Science

- UHV TPD
- SIMS
- end point detection in ion beam etch
- elemental imaging - surface mapping



Plasma Diagnostics

- plasma source characterization
- etch and deposition process reaction kinetic studies
- analysis of neutral and radical species



Vacuum Analysis

- partial pressure measurement and control of process gases
- reactive sputter process control
- vacuum diagnostics
- vacuum coating process monitoring

Focused helium and neon ion beam induced etching for advanced extreme ultraviolet lithography mask repair

Carlos M. Gonzalez, Rajendra Timilsina, Guoliang Li, Gerd Duscher, and Philip D. Rack^{a)}
Department of Materials Science and Engineering, University of Tennessee, Knoxville, Tennessee 37996-2200

Winand Slingenbergh, Willem F. van Dorp, and Jeff T. M. De Hosson
Department of Applied Physics, Zernike Institute for Advanced Materials, University of Groningen, Nijenborgh 4, 9747 AG Groningen, Netherlands

Kate L. Klein
Department of Mechanical Engineering, University of the District of Columbia, Washington, District of Columbia 20008

Huimeng M. Wu and Lewis A. Stern
Ion Microscopy Innovation Center LLC, Carl Zeiss Microscopy, One Corporation Way, Peabody, Massachusetts 01960

(Received 15 October 2013; accepted 26 February 2014; published 10 March 2014)

The gas field ion microscope was used to investigate helium and neon ion beam induced etching of nickel as a candidate technique for extreme ultraviolet (EUV) lithography mask editing. No discernable nickel etching was observed for room temperature helium exposures at 16 and 30 keV in the dose range of 1×10^{15} – 1×10^{18} He⁺/cm²; however, transmission electron microscopy (TEM) revealed subsurface damage to the underlying Mo-Si multilayer EUV mirror. Subsequently, neon beam induced etching at 30 keV was investigated over a similar dose range and successfully removed the entire 50 nm nickel top absorber film at a dose of $\sim 3 \times 10^{17}$ Ne⁺/cm². Similarly, TEM revealed subsurface damage in the underlying Mo-Si multilayer. To further understand the helium and neon damage, the authors simulated the ion–solid interactions with our EnvizION Monte-Carlo model, which reasonably correlated the observed damage and bubble formation to the nuclear energy loss and the implanted inert gas concentration, respectively. A critical nuclear energy density loss of ~ 80 eV/nm³ and critical implant concentration of $\sim 2.5 \times 10^{20}$ atoms/cm³ have been estimated for damage generation in the multilayer structure. © 2014 American Vacuum Society. [<http://dx.doi.org/10.1116/1.4868027>]

I. INTRODUCTION

Extreme-UV lithography (EUVL) is a next generation lithographic technique proposed to continue the trend of miniaturization in the nanoelectronics industry toward the 10 nm node.^{1–5} However, this high energy source (~ 13.5 nm wavelength) requires reflective masks, and thus, a new paradigm for the mask geometry, which consists of a multilayer dielectric mirror of two different materials with alternating refractive indices and thicknesses (2–5 nm), tuned to reflect a very narrow bandwidth. To protect the multilayer stack from oxidation and damage during mask processing, a thin protective layer (~ 2.5 nm) and a top EUV absorbing layer (~ 50 nm) is used to produce the pattern. Currently, ion-beam or magnetron sputter deposited Mo and Si multilayer stacks are most commonly used and studied for EUV lithography, which is capped by a thin ruthenium protective layer.^{6–10} The Mo/Si multilayer system is chosen due to its ability to act as a mirror in the 13.5 nm wavelength region with measured reflectivity as high as $\sim 70\%$. However, this peak reflectance occurs in a narrow spectral range where the reflectivity is only 10% at 13.0 nm and 13.7 nm wavelengths.¹¹ Hence, subtle variations in construction and in the

material properties, such as the formation of sillicides, can be deleterious to the mask fidelity. In another similar structure, the Mo/Be system outperforms slightly the Mo/Si, but Be is less desirable due to its toxicity.¹² Thin Ru barrier layers located in between the Mo and the Si layers have resulted in substantially less silicide formation at the interfaces.^{13,14} Other barrier materials such as a-C and B₄C have also been characterized.¹⁵ Au, W, Ta, and TaN have also been investigated for absorber films.¹⁶

Tantalum nitride (TaN) is the most commonly studied absorber layer; however, TaN spontaneously etches when exposed to XeF₂ during mask repair, thus requiring advanced passivation schemes.¹⁷ Nickel has superior EUV absorption^{2,3} over TaN and thus is being explored here as a candidate EUV absorber layer. To be a possible candidate material, there must be appropriate mask repair solutions. In 1985, Vietzke and Philipps¹⁸ investigated the high temperature erosion of Ni under 5 keV Ne⁺ irradiation. They found no enhanced release of nickel atoms exceeding physical sputtering and normal thermal sublimation. One of the leading mask repair solutions is electron beam induced etching; however, the low volatility of nickel halides has made it challenging to etch via focused electron beam induced etching. Hence, we have explored using the new gas field ion microscope as a possible strategy for repairing opaque nickel EUV defects.

^{a)}Present address: Center for Nanophase Materials Sciences, Oak Ridge National Laboratory, Oak Ridge, TN 37831; electronic mail: prack@utk.edu

Focused electron beam and focused ion beam (FIB) induced processing (IP) are well documented techniques.^{19,20} While gallium FIB IP (Ga-FIBIP) has been used historically in many applications,^{21,22} the resolution and gallium staining have made it obsolete as a mask repair tool for current and future state-of-the-art lithography masks.^{23,24} The enhanced resolution of the new gas field ion source (GFIS) microscope^{25–27} compared to liquid gallium ion sources and the fact that the species are inert gases makes it an intriguing option to study for mask repair. Focused helium or neon ions^{27–29} seem a logical choice for mask-repair applications because their low atomic mass will dissipate less of the ion energy through nuclear loss—most of it being lost to electronic interactions.³⁰ Recently, helium and neon focused ion beams have been shown to be capable of high-resolution additive deposition and subtractive etching^{31,32} that is superior to the gallium focused ion beam and in some cases with enhanced nanostructures, such as higher purity platinum nanowires, relative to electron beam induced deposition.^{32,33} Hydrogen ions (H^+ and H_2^+) generated via GFIS have also been characterized for EUVL mask repair. In this case, the authors concluded that, on actinic images, there was no difference between the repaired area and the non-repaired one.⁵ Livengood *et al.*^{31,34–39} have performed a dose-dependent study of He-beam induced damage in crystalline Si and Cu. Results demonstrated that no damage was observed up to a dose of $\sim 1 \times 10^{15}$ ions/cm². However, at a critical dose between 1×10^{15} – 5×10^{16} He⁺/cm², the defect density is sufficient to cause dislocations and amorphization. For doses higher than $\sim 5 \times 10^{16}$ He⁺/cm², helium is no longer soluble and the formation of subsurface nanobubbles is visible in transmission electron microscopy (TEM).^{34,40} These subsurface processes induce a measurable swelling in Si and Cu.

In order to optimize the optical properties during growth^{41,42} and to reduce stress in the multilayers^{43–45} the thermal stability of the Mo/Si stacks for EUV applications has previously been explored.⁴⁶ Interdiffusion between the layers and the formation of molybdenum silicide intermetallics deteriorates the optical properties of the mirror. Because industrial applications require high mirror quality and lifetime, the kinetics of interdiffusion have been extensively characterized.^{8,42,46} Importantly for stability of the mask, Bozorg-Grayeli *et al.*¹⁶ concluded that in a multilayer system such as Mo/Si, heat transfer and dissipation between layers is substantially degraded due to a thermal conductivity $100\times$ lower than for bulk values. This single fact may be responsible for enhanced silicidation at the interfaces.

According to the phase diagram, molybdenum silicides (especially: Mo₅Si₃, and hexagonal and tetragonal MoSi₂) form at temperatures at and above 700 K and result in a reduction of the lattice parameters. The volume of one MoSi₂ unit cell is smaller than the summed volumes of one Mo and two Si atoms ($Mo + 2Si \rightarrow MoSi_2$) by $\sim 27\%$. In the case of the widely investigated MoSi₂, its structure is hexagonal (h) initially and then transforms to tetragonal (t) with $a = 0.321$ nm and $c = 0.785$ nm. Thus, thermal treatments have been demonstrated to result in a contraction in Mo/Si

multilayers.^{8,46–48} Interestingly, it has been proposed that contraction due to electron-beam induced heating may be used to locally correct phase defects in mirrors.⁴⁶ Montcalm⁴⁴ reported a measurable change in reflectivity for a 30 s anneal at 100 °C and a 2% reduction in reflectivity after 30 s at ~ 300 °C. At increased temperatures, reflectance diminishes rapidly as volumetric contraction alters the optical properties of the mirror.^{49,50} TEM analysis revealed interlayer diffusion after a 1-h anneal at 316 °C.⁸ As previously mentioned, to counteract interdiffusion, several different types of diffusion barriers have been proposed.^{51–53}

In this paper, the He and Ne ions are explored as a method for etching a 50 nm thick nickel absorber layer on a Mo-Si multilayer EUV mask. Atomic force microscopy (AFM) and TEM analyses have been performed to investigate the induced changes as a function of dose in the Mo-Si multilayer stack. The experimental results are subsequently simulated with the EnvizION Monte-Carlo modeling program^{54,55} in which we simulate the nickel sputtering process as well as the damage caused by the nuclear energy loss and implanted inert gas species.

II. EXPERIMENTAL METHODS

The Ru-capped (2.5 nm) m-Mo/a-Si (40×7 nm) bilayer stacks were prepared on silicon wafers by Lawrence Livermore National Laboratory (LLNL) using an ion beam sputtering process. Two sets of samples were prepared, namely; one with a 50 nm nickel top absorbing layer and another without the nickel.

The room temperature helium exposures were performed with a Zeiss Orion microscope at the National Institute of Standards Technology (NIST). Rectangles of $0.5 \mu\text{m} \times 5.0 \mu\text{m}$ were scanned with a 2 pA current and a 1 μs dwell time in a serpentine fashion at 16 and 30 kV. The doses ranged from 3×10^{14} to 1×10^{19} He⁺/cm². Scanning electron microscopy imaging of the helium and neon exposures were performed with a Zeiss Auriga Cross Beam and with an FEI Nova Lab 600 Dual Beam. TEM samples were prepared with the Auriga Cross Beam system and a Kleindiek micromanipulator. TEM analysis was done with a Zeiss Libra 200MC. Energy dispersive x-ray spectroscopy (EDXS) was performed with the Bruker Quantax system attached to the Libra 200. AFM measurements were performed in tapping mode with a Veeco Dimension 3100.

The neon exposures at room temperature were made at Carl Zeiss Microscopy in Peabody, MA, using an Orion gas field ion microscope. Rectangles of $0.1 \mu\text{m} \times 1.5 \mu\text{m}$ were scanned with a 30 kV beam, a current of 0.5 pA, a 0.3 μs dwell time, a 10 μs refresh time, 1 nm \times 1 nm spacing (101 \times 1501 dwell points) in a serpentine fashion and at 0° incidence. A set of eight rectangular exposures was patterned using a Fibics NPVE pattern generator. The doses ranged from 0.1 to 1.5 nC/ μm^2 in increments of 0.2 nC/ μm^2 (6.25×10^{16} to 9.38×10^{17} Ne⁺/cm²). At the highest dose of 1.5 nC/ μm^2 , the total duration of the exposure run was recorded as 52 s (152 ms/frame). Increasing doses were realized by increasing the number of loops as follows: 23, 69, 115, 162,

208, 254, 300, and 346 for 0.1, 0.3, 0.5, 0.7, 0.9, 1.1, 1.3, and 1.5 nC/ μm^2 , respectively. The chamber base pressure without neon was 3.97×10^{-7} Torr, and after the neon valve was opened, the pressure stabilized at 2.5×10^{-6} Torr. The source trimer was stable during the entire test and did not require new tip formation. Milling was carried out at a working distance of 6.1 mm and with a $20 \mu\text{m}$ aperture.

SRIM/TRIM⁵⁶ simulations were initially performed in order to obtain predictive information for the experiment. Subsequently Monte-Carlo ion–solid simulations were performed using our EnvZION simulation. Exposures of 100 000 and 150 000 ions per run were simulated for helium and for neon, respectively. The raster grid was $10 \text{ nm} \times 10 \text{ nm}$, with 1 nm FWHM pixels, 2 nm pixel spacing, and a dwell time of $0.5 \mu\text{s}$. In order to simulate the multilayer, each scattering event is randomized to be either from Mo or Si in accordance with their volumetric ratio in the structure (taken as 60% Mo and 40% Si). The binding energy of nickel was assumed to be 4.46 eV, which corresponds to its heat of sublimation.

III. RESULTS AND DISCUSSION

A. Focused helium beam exposures

TEM cross-sectional images were obtained for doses ranging from 1×10^{16} to 1×10^{18} He^+/cm^2 and for two beam energies, 16 and 30 keV. Figure 1 shows TEM micrographs of the exposed Ni-Mo/Si multilayer films as a function of increasing dose. The results demonstrate that the film stack contracts slightly with increasing dose, while there is no evidence of nickel etching. Also evident is a clear “beam interaction region,” which emerges at the 5×10^{16} dose and is more obvious at the dose of $\sim 1 \times 10^{17}$ ions/ cm^2 . Finally, Figs. 1(e) and 1(j) shows significant swelling at a higher dose of 1×10^{18} ions/ cm^2 with noticeable bubble formation. Note that the bottom silicon substrates are aligned from (a) to (j), indicating the small changes in the thickness of the multilayer stack. Specifically, there is a series of contractions up to the 5×10^{16} dose, a smaller increase at 1×10^{17} (onset of swelling), followed finally by a dramatic $\sim 180 \text{ nm}$

expansion at 1×10^{18} He^+/cm^2 . See supplementary material in Ref. 57 for AFM data with measured heights as a function of helium ion doses. Aside from the contractions and swelling, we also observe (and measured via AFM) slight depressions, which indicate that subsurface contractions have taken place. The depressions are dose dependent and TEM analysis rules out ion-beam induced surface sputtering since there is no measurable reduction in the thickness of the Ni top layer. The depressions are consistent with silicidation as more energy is deposited with higher doses. This increases the probability that the required activation energy for Mo/Si interdiffusion is overcome and hence the stack densifies. These observations are consistent with the results of Livengood *et al.* and can be explained by nuclear energy loss of the helium atoms causing beam induced mixing. At sufficiently high concentrations this leads to the formation of helium nanobubbles. Bubbling has been documented previously, especially in studies involving helium irradiation effects on silicon and silica substrates.^{40,58} It is clear from these micrographs that helium, under these conditions, is not viable for nickel etching.

A closer inspection of the multilayer stack after exposure [Fig. 2(a)] reveals a thinning down of the silicon layer and intermixing of the Mo/Si layers, which is also shown in the energy filtered TEM image [Fig. 2(b)]. The intermixing is attributed to the nuclear energy loss via either thermal spike or knock-on processes. Heating is possible and exacerbated since interplanar heat transfer is hindered by the many interfaces present in such multilayer systems. Moreover, bubbles are observed in the amorphous silicon layer (bright regions) within the stack [Fig. 2(c)]. The observation that the bubble formation is preferential to the silicon layers (as seen in 2d) may be explained by a lower solubility limit for helium in silicon. Additionally, amorphous silicon (50–100 GPa and 0.13 GPa)⁵⁹ has significantly lower modulus of elasticity and yield strength, with respect to molybdenum (329 GPa and 0.45 GPa). Hence, we expect Si to elastically deform more under the same internal stress and plastically deform at a lower dose than Mo due to strains introduced by the implanted helium atoms.

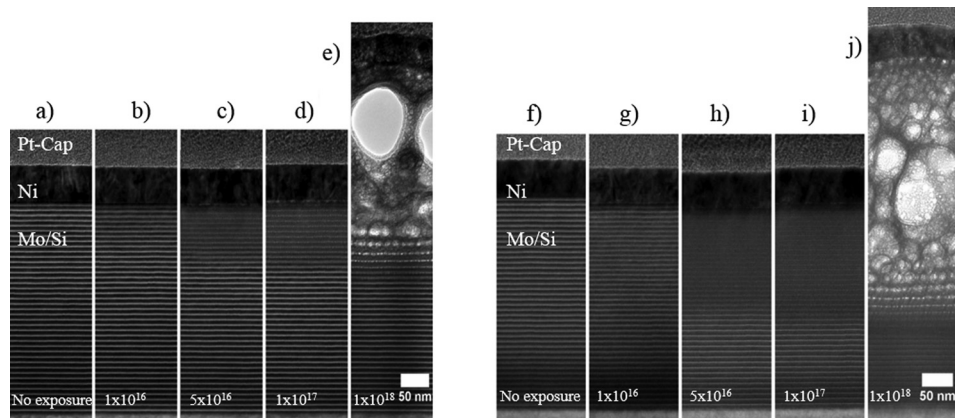


FIG. 1. TEM cross-sectional micrographs of nickel on top of a Mo/Si multilayer stack that was exposed to 16 (a)–(e) and to 30 (f)–(j) keV helium ion energies in doses ranging from 1×10^{16} to 1×10^{18} ions/ cm^2 . The direction of the incident He^+ beam is normal to the top side of each panel from (a) to (j). Ions travel from top down across the image until they come to rest. The silicon substrate is seen on the bottom of each micrograph and aligned with the adjacent images.

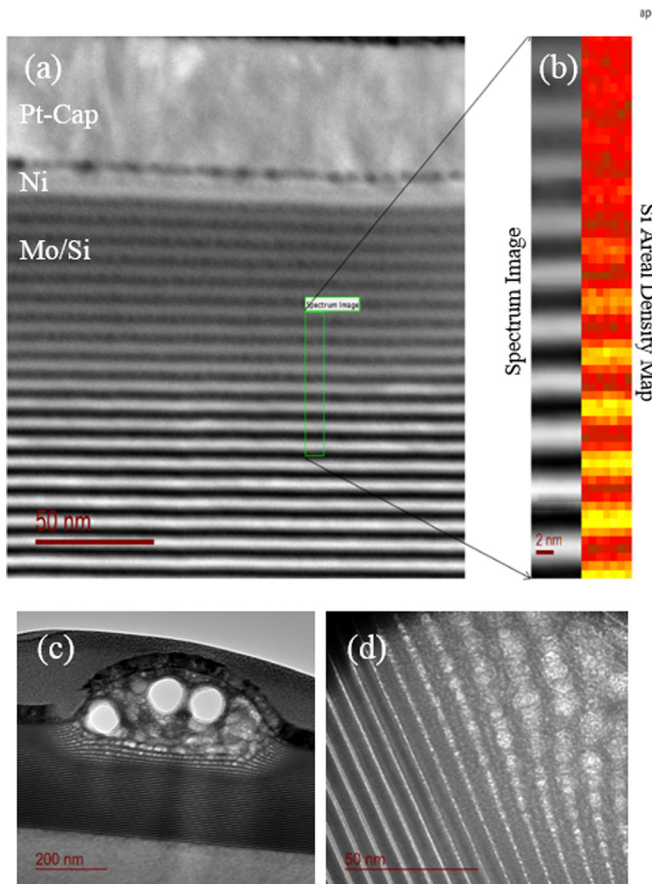


FIG. 2. (Color online) High magnification Z-contrast image of a 30 keV, 1×10^{17} He^+/cm^2 exposure (a). Z-contrast image (left) and silicon EELS map (right) (b). At higher doses, such as 1×10^{18} He^+/cm^2 severe bubbling is observed which originates preferentially in the silicon layer of the stack, as shown in (c) and (d).

The micrograph in Fig. 3(a) makes it quite evident that the silicon layers nearest to the nickel top layer were consumed and thinned. The top multilayers (damaged) are more diffuse and less well-defined than those deeper in the

structure (undamaged). EELS analysis [Fig. 3(b)] at two different locations in the multilayer stack indicate spectra that the unaffected region are characteristic of a-Si and the damaged region is characteristic of reacted silicon, which is suggestive of silicide formation. Energy transfer through direct knock-on is more probable for Si than Mo due to the relatively low atomic mass difference between silicon and helium. Additionally, the heat of sublimation for Si (359 kJ/mol) is much lower than Mo (617 kJ/mol), thus it requires less energy to dislodge Si from its lattice position than Mo. Hence, silicon is expected to preferentially be knocked out of its lattice relative to molybdenum and thus create vacancies for the helium atoms to occupy. The diffuse appearance of the silicon layers closest to the beam impingement surface indicates that many silicon atoms have been scattered, most likely forward as the momentum vector of the incident ions points downward deeper into the stack.

B. Helium ion–solid modeling

In order to better understand the observed damage induced by the helium irradiation, we simulated the energy loss associated with the 16 and 30 keV helium ion with our EnvizION simulation. From AFM and TEM imaging, it is evident that the depth of the depression as well as the damaged region is greater for the 30 keV sample than 16 keV at the same dose. These observations are supported by the simulations. Silicide formation may be thermally induced or via knock-on collisions as described earlier. In both cases, the nuclear energy loss is responsible; thus, we can correlate the nuclear energy density loss to the observed damage profiles. In Fig. 4, the volumetric electronic and nuclear losses in eV/nm^3 for He^+ at 30 kV have been mapped. A simulation run of $\sim 100\,000$ helium ions raster scanned over a $10 \text{ nm} \times 10 \text{ nm}$ area corresponds to an experimental dose of 1×10^{17} ions/ cm^2 . Near the surface of impingement, the ratio at the maximum energy loss between electronic and nuclear stopping is ~ 32 , which is consistent with the lack of

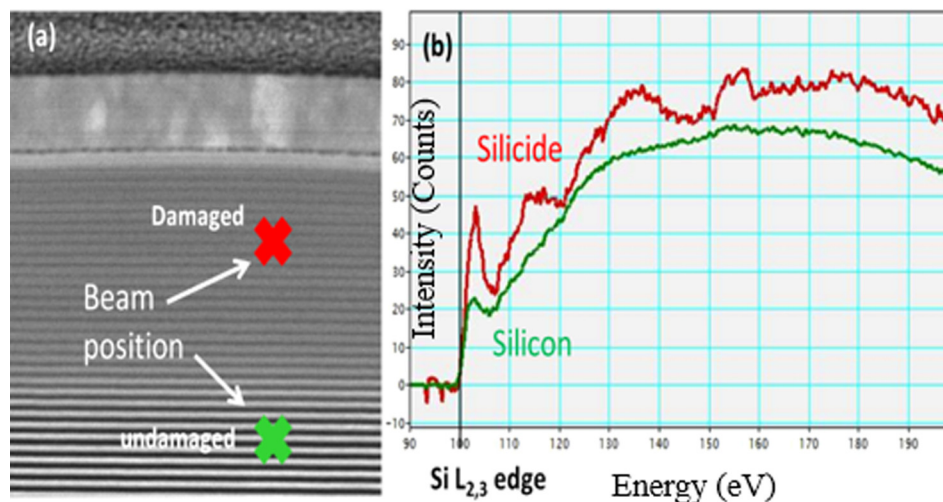


FIG. 3. (Color online) Z-contrast TEM image illustrating two comparable EELS spectra taken in the Mo/Si multilayers. The lower 'x' mark in (a) represents an undamaged region, while the top mark (nearest to top surface) represents a damaged region. The corresponding EELS spectra are shown in (b). The Si $L_{2,3}$ edge in the undamaged region corresponds to typical a-Si, while in the damaged region it shows characteristic silicide signatures.

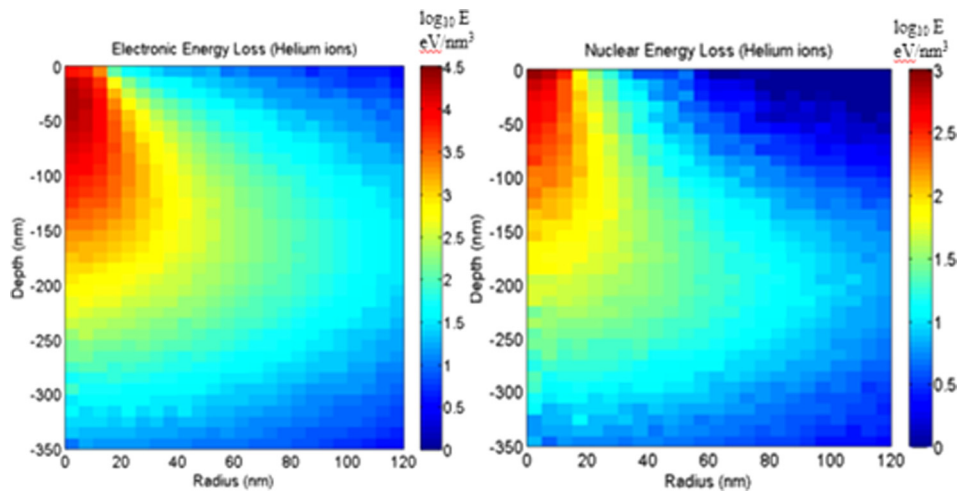


FIG. 4. (Color online) Simulated electronic and the nuclear volumetric energy losses for helium ions at 30 keV at a dose of 1×10^{17} ions/cm².

measurable sputtering of nickel by helium. Examining the simulated depth of the nuclear stopping energy density reveals good agreement with the observed damage profile in the TEM images and allows us to estimate an energy threshold for the observed damage. The 16 keV simulations were performed and, as shown also in Fig. 5(a), the simulated

nuclear energy threshold of ~ 80 eV/nm³ correlates well with the damage threshold for the 1×10^{17} He ions/cm² dose. Similarly, the simulated nuclear energy loss for 30 keV He⁺ shows a clear range down to ~ 180 nm as can be seen also in Fig. 5(b) below. Beyond this depth, damage (halo) is not recognizable. At 30 keV, the most significant nuclear loss

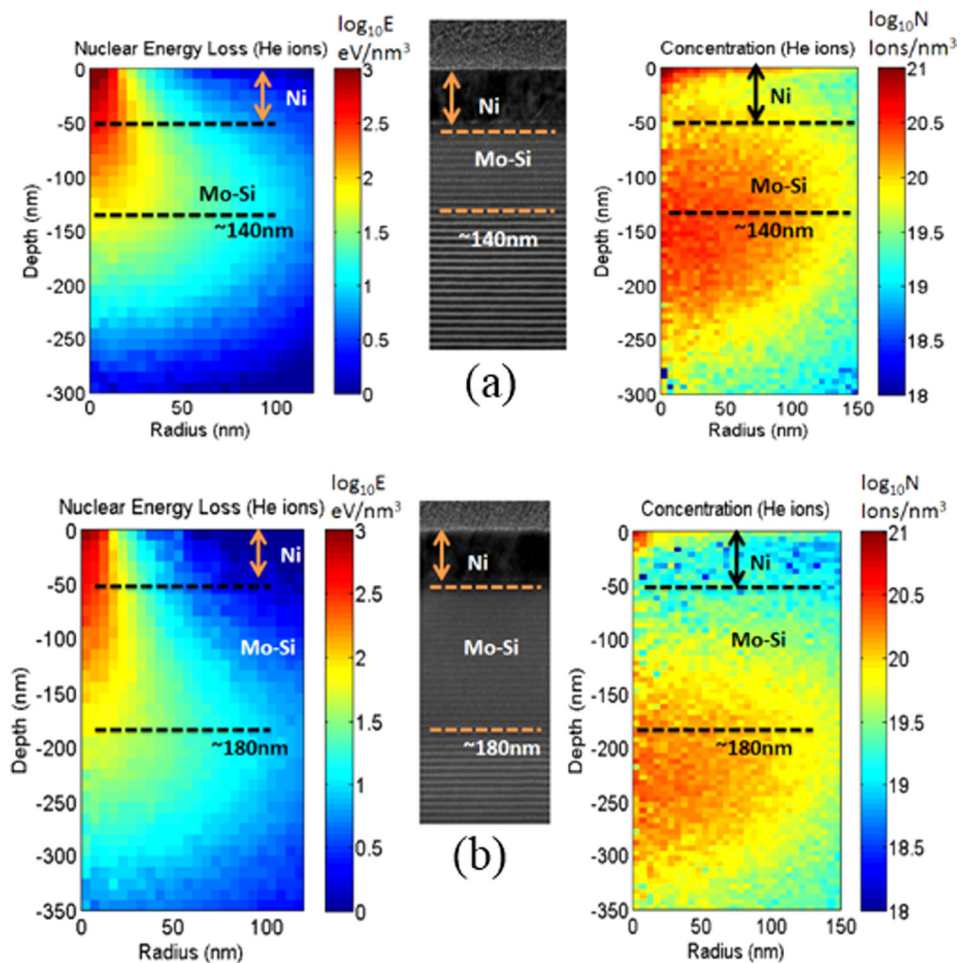


FIG. 5. (Color online) Simulated nuclear energy loss (left) and the resultant helium implant concentrations (on right) are compared to the experimental TEM micrograph exposed to 16 keV at a dose of 2×10^{17} He⁺/cm². In (b), the same as in (a), but for 30 keV He⁺.

remains close to the top surface and within the nickel layer. Based on these results, the nuclear energy loss near the top of the Mo/Si stack is still sufficient to induce some intermixing of Si and Mo. In this region, a critical energy density for silicidation has been estimated from the simulation to be $\sim 80\text{--}100\text{ eV/nm}^3$. As mentioned before, greater nuclear loss occurs within the nickel top layer; however, the ductile metal film can apparently accommodate the energy loss in part by some observed grain growth. At $1 \times 10^{17}\text{ He}^+/\text{cm}^2$, a critical implant concentration for damage has been determined to be $\sim 2.5 \times 10^{20}\text{ He/cm}^3$ (in close agreement with data for He in Si published by Nguyen *et al.*). This corresponds to $\sim 0.5\%$ He in Si or a solubility of near 1 He: 200 Si. This agrees with Reutov and Sokhatski,⁴⁰ where bubbles caused by a 17 keV He⁺ beam in Si constituted $\sim 1.6\%$ of the volume. In our study, a 0.5% He content had not yet induced the formation of nanobubbles in Mo/Si.

C. Focused neon beam exposures

Figure 6 shows sequential TEM cross-section images (a)–(h) for neon ion doses ranging from 0.1 to 1.5 nC/ μm^2 (or $6.25 \times 10^{16}\text{--}9.34 \times 10^{17}\text{ Ne}^+/\text{cm}^2$). Clearly, nickel etching has progressively taken place. In our room temperature study, the nickel milling efficiency using a 0.5 pA beam was calculated to be $0.57\text{ }\mu\text{m}^3/\text{nC}$, yielding an estimated sputter yield of 1.5 Ni/Ne⁺. It took only 17.6 s to mill through a 50 nm top absorber nickel layer. Aspect ratios (A.R.) follow a near-linear dependence on the neon dose, reaching 2.0 at the highest dose in these experiments. See supplementary material in Ref. 57 for a plot of A.R. versus dose for Ne⁺. Nickel sputtering already occurs at the lowest experimental dose of $6.25 \times 10^{16}\text{ Ne}^+/\text{cm}^2$. Furthermore, the TEM images reveal similar subsurface damage as seen in the helium exposures. The dose at which bubbling occurs is

lower, however ($<6.25 \times 10^{16}\text{ Ne}^+/\text{cm}^2$ versus $1 \times 10^{18}\text{ He}^+/\text{cm}^2$). The neon damage region is not as deep when compared with helium, but the damage appears more severe because neon has a smaller interaction volume. The formation of neon nanobubbles is evident and several regions are discernible; ranging first from: (1) a narrow band with small, collapsing bubbles near the free surface, to (2) a wider belt containing larger bubbles, followed by (3) another band of smaller bubbles, and finally to (4) a damage “halo” revealing Mo/Si intermixing. This is in agreement with the pattern reported by Nguyen *et al.*⁵⁸ for 50 keV He⁺ in crystalline Si, and by Oliviero *et al.*⁶⁰ for 50 keV Ne⁺ also in c-Si. Small bubbles or platelets transform into larger bubbles by loop punching and later by Ostwald ripening. It is very likely that all the gas remains inside the bubble layer during this coarsening process. The bubbles are over pressurized and growth of cavities by interstitial emission or vacancy capture will be higher in metals, but rather slow in Si where even at high temperatures it will take considerable time.

EDXS analysis performed in the Libra 200MC instrument on the $0.7\text{ nC}/\mu\text{m}^2$ sample (200 keV electron beam energy) detected the following elements: Ni, Mo, Si, Ru, and Ne from the sample, and Pt and Cu from the protection layer on the sample and the mounting grid, respectively. At this dose, the nickel overlayer has already been removed, and the features reside mostly within the now damaged Mo/Si stack volume. The analysis shows that higher counts for neon are present below the largest nanobubble, directly under the incident Ne⁺ beam trajectory during ion irradiation. A slightly larger count at 850 eV may be due to embedded neon gas. This energy for Ne K α is the same as for Ni L α . However, at 7.47 keV, for Ni K α , no significant counts and differences between three test points were detected. It has been concluded that Ni does not forward scatter deeper into the structure as the etching process mills across the top absorber

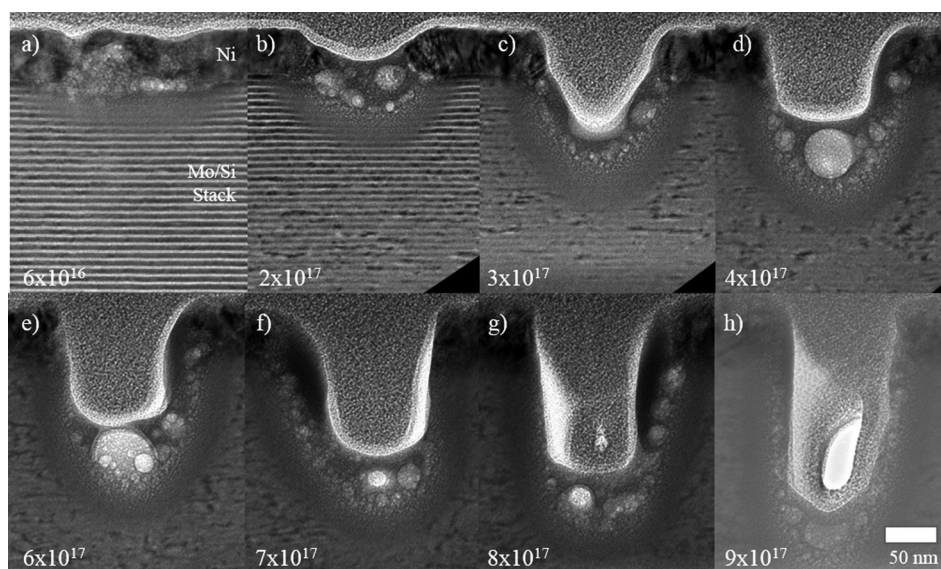


FIG. 6. Sequential TEM cross-sections illustrating the progression in etch depth and the formation of cavities below the surface. The Ne⁺ beam energy was 30 keV with doses ranging from 6.25×10^{16} (or $0.1\text{ nC}/\mu\text{m}^2$) for a) to $9.38 \times 10^{17}\text{ Ne}^+/\text{cm}^2$ (or $1.5\text{ nC}/\mu\text{m}^2$) for h). The direction of the Ne⁺ beam is normal to the top side of each panel from (a) to (h). Ions travel from top down across the image until they come to rest.

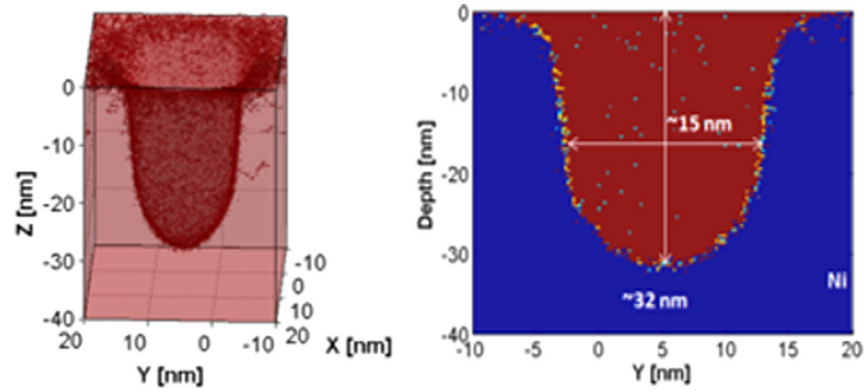


Fig. 7. (Color online) 3D and 2D sputter profiles for Ne^+ in Ni at 30 keV and $\sim 2 \times 10^{17}$ ions/cm² (using a 10 nm \times 10 nm exposure area).

layer. See supplementary material in Ref. 57 for a summary of EDXS data. Dense nanobubbles with a concentration up to 1×10^{23} atoms/cm³ have been reported to have internal pressures between 5 and 8 GPa in the 300–1000 K range. This remains below the elemental elastic moduli for Ni, Mo, and Si. Already starting at room temperature in metals and at higher temperature in Si, the first phase of helium/neon release is ascribed to dissociation of small noble gas/vacancy complexes, and in the second phase of release, it is ascribed to noble gasses permeating from a bubble layer to the sample surface. The fact that bubbles are over-pressurized and that release does not occur from single bubbles, but from a bubble layer should be taken into account in a full physical description of the process.⁶¹

D. Neon ion–solid modeling

EnvizION neon simulations were also performed to better understand the experimental results. For the neon simulations, we utilized a recent addition to the simulation, which includes recoil and sputtering to reveal the evolving surface.^{54,55} To validate our EnvizION simulation for neon, we performed energy dependent sputter yield curves for nickel. These show good agreement with experimental values. The calculated sputter yield at 30 keV is 2.0 Ni/Ne⁺, which is a slight overestimation of the measured sputter yield of 1.5. See supplementary material in Ref. 57 for experimental and simulated sputter yields. We attribute this discrepancy to

factors that slow down the net removal of nickel such as the subsurface damage (effectively increasing the interaction volume and lowering the nuclear energy loss) and redeposition on the via sidewalls.

Figure 7 shows 3D and 2D sputter profiles of the nickel top layer at a low dose. It must be noted that while in this case the neon peak concentration of implanted atoms remains within the nickel layer, a substantial amount of neon reaches the Mo/Si stack to about 100 nm deep, or 50 nm inside the Mo/Si stack. The etch cross section for an EnvizION run of 150 000 neon ions (in a 10 nm \times 10 nm area) resembles the experimental data for a dose of $\sim 2 \times 10^{17}$ Ne⁺/cm² at 30 keV. At this dose and energy, approximately 32 nm of the 50 nm nickel layer is removed. This etch depth agrees with the 33 nm measured experimentally in the TEM. Beneath the sputtered depth the implanted distribution tails down into the Mo/Si stack. Noticeably, the experimental via width is wider than the beam raster area. Experimentally, the 100 nm wide scan yielded ~ 136 nm opening in the nickel layer. The EnvizION simulation used a 10 \times 10 nm² smaller exposed area (for shorter simulation times), which yielded a larger 15 \times 15 nm² sputter etched via, demonstrating similar broadening due to the beam tails and interaction volume.

In Fig. 8, the volumetric nuclear energy loss and final concentrations for neon at 30 keV are compared side by side with the actual TEM cross section micrograph at the same dose. In this case, it is notable that a high nuclear

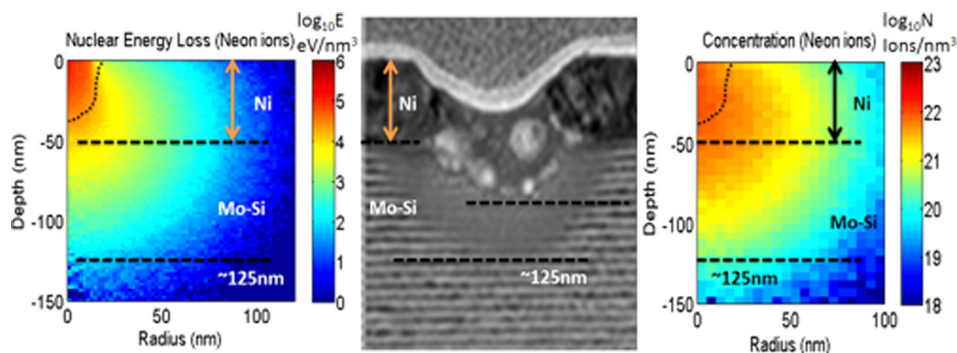


Fig. 8. (Color online) Simulated nuclear energy loss (left) and the resultant neon implant concentrations (on right) are compared to the experimental TEM micrograph exposed to 30 kV at a dose of 2×10^{17} Ne⁺/cm².

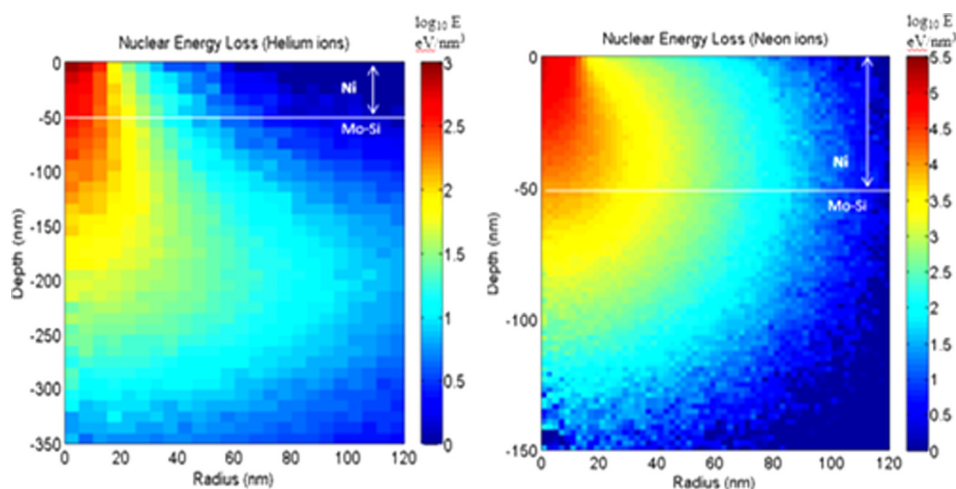


Fig. 9. (Color online) Comparison of the simulated volumetric nuclear energy losses of helium and of neon at 30 keV. EnvizION runs of 100 000 ions corresponded to a dose of $\sim 1 \times 10^{17}$ He⁺/cm², and of 150 000 ions corresponded to a dose of $\sim 2 \times 10^{17}$ Ne⁺/cm².

energy loss region extends beyond the nickel layer into the Mo/Si multilayer. The damaged region at $\sim 2 \times 10^{17}$ Ne⁺/cm² includes nanobubbles that are present [Fig. 8(a)] in the nickel, but concentrated near the interface of the Mo/Si stack, and [Fig. 8(b)] within the stack to a shallow depth of about 50 nm. Here, it is clear that the peak energy loss is taking place within the Ni, where it causes physical sputtering, yet substantial nuclear energy loss also extends into the Mo/Si region down to ~ 100 nm from the original top surface of the nickel (experimentally, the halo extends to ~ 116 nm). For etching in nickel to take place, the simulation predicts a minimum nuclear energy density of ~ 30 keV/nm³. Bubbling is observed and is attributed to the implanted neon at concentrations on the order of 10^{21} Ne/cm³; while conversely, no damage is again discernable below 80 eV/nm³.

Figure 9 shows a marked difference in nuclear energy losses between helium and neon at nearly the same dose ($1\text{--}2 \times 10^{17}$ ions/cm²). Clearly, helium deposits its energy deeper and over a larger volume than neon. However, near the impingement top surface, the ratio between the peak nuclear losses of Ne:He at 30 keV is ~ 100 , thus leading to the observed sputtering of nickel by neon.

IV. CONCLUSIONS

We have studied the feasibility of etching nickel EUV absorber layers on Mo/Si multilayers via focused helium and neon ion beam processing. Helium ion beams at both 16 and 30 keV do not etch the nickel absorber layer and TEM imaging reveals unwanted intermixing of the underlying Mo/Si EUV reflector layers. At doses below 1×10^{17} He⁺/cm², a progressive contraction consistent with molybdenum silicide formation is observed. At higher doses, nanobubble formation occurs and causes swelling that can be attributed to peak implant concentrations in excess of 10^{21} He/cm³. Ion–solid Monte Carlo simulations at both 16 and 30 keV reveal that the damage can be correlated to the nuclear energy loss of the helium ion beam and that the Mo/Si intermixing is due to either knock-on collisions, a thermal spike or a combination thereof.

For neon ion beam induced exposures at 30 keV, the nickel absorber layer is effectively etched due to higher nuclear energy loss in the near surface region. TEM images reveal a subsurface damage profile consisting of nanobubbles and an extended region of apparent Mo/Si intermixing occurs. The measured sputtering rate of ~ 1.5 nickel atoms/neon ion is comparable to the simulated sputtering rate of two nickel atoms/neon ion. Ion–solid Monte Carlo simulations reveal that nanobubbles form at much lower doses for neon due to the shorter range and thus higher neon implant concentrations. Nanobubble formation is correlated to concentrations exceeding 10^{21} Ne/cm³. Furthermore, the observed damage region beneath the neon nanobubbles is attributed to knock-on or thermal spike induced intermixing of the Mo/Si layers due to the nuclear energy loss.

ACKNOWLEDGMENTS

P.D.R. and C.G. would like to acknowledge the Semiconductor Research Corporation (SRC) and INTEL Corporation for supporting this work (contract: SRC-2012-In-2310). Our special gratitude goes to Ted Liang for his mentoring and meaningful discussions. The authors do thank Eric M. Gullikson of LLNL for preparing the mirror structures used in the experiments. K.K. and W.S. would like to thank Andras Vladár at NIST for use of the Orion for helium exposures. Furthermore, R.T. and P.D.R. acknowledge that the EnvizION simulation was further supported by the Semiconductor Research Corporation via contract #2122 (Bob Havemann program manager). C.G. would like to thank John R. Dunlap for assisting on some of the TEM and EDXS analysis. Finally, a portion of this work was research was conducted at the Center for Nanophase Materials Sciences, which was sponsored at Oak Ridge National Laboratory by the Scientific User Facilities Division, Office of Basic Energy Sciences, US Department of Energy.

¹R. H. Stulen and D. W. Sweeney, *IEEE J. Quantum Electron.* **35**, 694 (1999).

²A. Lyons, R. Teki, and J. Hartley, *Proc. SPIE* **8322**, 83221X (2012).

- ³H. J. Levinson, P. Mangat, T. Wallow, L. Sun, P. Aukmann, and S. Meyers, *Proc. SPIE* **8679**, 867916 (2013).
- ⁴R. Peeters *et al.*, *Proc. SPIE* **8679**, 86791F (2013).
- ⁵F. Aramaki *et al.*, *Proc. SPIE* **7969**, 79691C (2011).
- ⁶T. W. Barbee, S. Mrowka, and M. C. Hettrick, *Appl. Opt.* **24**, 883 (1985).
- ⁷S. P. Vernon, D. G. Stearns, and R. S. Rosen, *Opt. Lett.* **18**, 672 (1993).
- ⁸R. S. Rosen, D. G. Stearns, M. A. Viliardos, M. E. Kassner, S. P. Vernon, and Y. D. Cheng, *Appl. Opt.* **32**, 6975 (1993).
- ⁹R. S. Rosen, M. A. Viliardos, M. E. Kassner, D. G. Stearns, and S. P. Vernon, *Proc. SPIE* **1547**, 212 (1992).
- ¹⁰J. M. Slaughter *et al.*, *J. Appl. Phys.* **76**, 2144 (1994).
- ¹¹T. Heil and M. Lowisch, *Manuf. Technol., Photonik Int.* **2**, 70 (2008).
- ¹²M. Singh and J. J. M. Braat, *Proc. SPIE* **3997**, 412 (2000).
- ¹³T. G. Kim, J. Ahn, S. Y. Lee, and J. G. Park, *J. Korean Phys. Soc.* **45**, 1229 (2004).
- ¹⁴S. Y. Lee, T. G. Kim, and J. Ahn, *J. Korean Phys. Soc.* **43**, 826 (2003).
- ¹⁵S. Braun, H. Mai, M. Moss, R. Scholz, and A. Leson, *Jpn. J. Appl. Phys.* **41**, 4074 (2002).
- ¹⁶E. Bozorg-Grayeli, Z. J. Li, M. Ashghi, G. Delgado, A. Pokrovsky, M. Panzer, D. Wack, and K. E. Goodson, *J. Appl. Phys.* **112**, 083504 (2012).
- ¹⁷M. G. Lassiter, T. Liang, and P. D. Rack, *J. Vac. Sci. Technol. B* **26**, 963 (2008).
- ¹⁸E. Vietzke and V. Philipps, *J. Nucl. Mater.* **337**, 1024 (2005).
- ¹⁹I. Utke, P. Hoffmann, and J. Melngailis, *J. Vac. Sci. Technol. B* **26**, 1197 (2008).
- ²⁰S. J. Randolph, J. D. Fowlkes, and P. D. Rack, *Crit. Rev. Solid State* **31**, 55 (2006).
- ²¹Y. Drezner, D. Fishman, Y. Greenzweig, and A. Raveh, *J. Vac. Sci. Technol. B* **29**, 011026 (2011).
- ²²A. Reguer, F. Bedu, J. Tonneau, H. Dallaporta, M. Prestigiacomo, A. Houel, and P. Sudraud, *J. Vac. Sci. Technol. B* **26**, 175 (2008).
- ²³I. Utke, V. Friedli, M. Purrucker, and J. Michler, *J. Vac. Sci. Technol. B* **25**, 2219 (2007).
- ²⁴N. Yao and A. K. Epstein, *Microsc.: Sci. Technol. Appl. Educ.* **3**, 2190 (2010).
- ²⁵W. B. Thompson, J. Notte, L. Scipioni, M. Ananth, L. Stern, C. Sanford, and S. Ogawa, *ISTFA 2009: Proceedings of the 35th International Symposium for Testing and Failure Analysis* (ASM International, San Jose, CA), p. 339.
- ²⁶L. Scipioni, P. Alkemade, V. Sidorkin, P. Chen, D. Maas, and E. van Veldhoven, *Am. Lab.* **41**, 26 (2009).
- ²⁷B. Ward, J. A. Notte, and N. P. Economou, *Photon. Spectra* **41**, 68 (2007).
- ²⁸M. Ananth, L. Stern, J. Notte, L. Scipioni, C. Huynh, and D. Ferranti, *Proc. SPIE* **8036**, 80360M (2011).
- ²⁹J. Maas, E. van Veldhoven, and P. F. A. Alkemade, *MRS Proc.* **1354**, mrs11-1354-ii03-03 (2011).
- ³⁰D. C. Joy, R. Ramachandra, and B. Griffin, *Microsc. Microanal.* **15**, 648 (2009).
- ³¹F. H. M. Rahman, S. McVey, L. Farkas, J. A. Notte, S. D. Tan, and R. H. Livengood, *Scanning* **34**, 129 (2012).
- ³²L. S. W. Thompson, H. Wu, D. Ferranti, D. Xia, F. Khanom, P. D. Rack, and C. Gonzalez, *ISTFA 2012: Proceedings of the 38th International Symposium for Testing and Failure Analysis* (ASM International, Phoenix, AZ), p. 455.
- ³³H. M. Wu *et al.*, *Nanotechnology* **24**, 175302 (2013).
- ³⁴R. Livengood, S. Tan, Y. Greenzweig, J. Notte, and S. McVey, *J. Vac. Sci. Technol. B* **27**, 3244 (2009).
- ³⁵S. D. Tan, R. H. Livengood, R. Hallstein, D. Shima, Y. Greenzweig, J. Notte, and S. McVey, *ISTFA 2011: Proceedings of the 37th International Symposium for Testing and Failure Analysis* (ASM International, San Jose, CA), p. 40.
- ³⁶S. D. Tan, R. Livengood, P. Hack, R. Hallstein, D. Shima, J. Notte, and S. McVey, *J. Vac. Sci. Technol. B* **29**, 06F604 (2011).
- ³⁷R. H. Livengood, Y. Greenzweig, T. Liang, and M. Grumski, *J. Vac. Sci. Technol. B* **25**, 2547 (2007).
- ³⁸S. D. Tan, R. Livengood, D. Shima, J. Notte, and S. McVey, *J. Vac. Sci. Technol. B* **28**, C6F15 (2010).
- ³⁹Y. Drezner, Y. Greenzweig, D. Fishman, E. van Veldhoven, D. J. Maas, A. Raveh, and R. H. Livengood, *J. Vac. Sci. Technol. B* **30**, 041210 (2012).
- ⁴⁰K. J. Abrams, J. A. Hinks, C. J. Pawley, G. Greaves, J. A. van den Berg, D. Eyidi, M. B. Ward, and S. E. Donnelly, *J. Appl. Phys.* **111**, 083527 (2012).
- ⁴¹A. Kloidt, K. Nolting, U. Kleineberg, B. Schmiedeskamp, U. Heinzmann, P. Muller, and M. Kuhne, *Appl. Phys. Lett.* **58**, 2601 (1991).
- ⁴²H. J. Voorma, E. Louis, N. B. Koster, and F. Bijkerk, *J. Appl. Phys.* **83**, 4700 (1998).
- ⁴³R. R. Kola, D. L. Windt, W. K. Waskiewicz, B. E. Weir, R. Hull, G. K. Celler, and C. A. Volkert, *Appl. Phys. Lett.* **60**, 3120 (1992).
- ⁴⁴C. Montcalm, *Opt. Eng.* **40**, 469 (2001).
- ⁴⁵T. Leisegang, D. C. Meyer, A. A. Levin, S. Braun, and P. Paufler, *Appl. Phys. A* **77**, 965 (2003).
- ⁴⁶P. B. Mirkarimi, D. G. Stearns, S. L. Baker, J. W. Elmer, D. W. Sweeney, and E. M. Gullikson, *J. Appl. Phys.* **91**, 81 (2002).
- ⁴⁷H. Azuma, A. Takeichi, I. Konomi, Y. Watanabe, and S. Noda, *Jpn. J. Appl. Phys.* **32**, 2078 (1993).
- ⁴⁸D. L. Windt, *J. Vac. Sci. Technol. A* **18**, 980 (2000).
- ⁴⁹M. Wedowski, J. H. Underwood, E. M. Gullikson, S. Bajt, J. A. Folta, P. A. Kearney, C. Montcalm, and E. Spiller, *Proc. SPIE* **3997**, 83 (2000).
- ⁵⁰T. Feigl, H. Lauth, S. Yulin, and N. Kaiser, *Microelectron. Eng.* **57–58**, 3 (2001).
- ⁵¹S. A. Bajt and D. G. Stearns, *Appl. Opt.* **44**, 7735 (2005).
- ⁵²H. Takenaka, H. Ito, T. Haga, and T. Kawamura, *J. Synchrotron Radiat.* **5**, 708 (1998).
- ⁵³T. Bottger, D. C. Meyer, P. Paufler, S. Braun, M. Moss, H. Mai, and E. Beyer, *Thin Solid Films* **444**, 165 (2003).
- ⁵⁴R. Timilsina, D. A. Smith, and P. D. Rack, *Nanotechnology* **24**, 115302 (2013).
- ⁵⁵R. Timilsina and P. D. Rack, *Nanotechnology* **24**, 495303 (2013).
- ⁵⁶*The Stopping Range of Ions in Solids*, edited by J. F. Ziegler, J. P. Biersack, and U. Littmark (Pergamon, New York, 1985), p. 13.
- ⁵⁷See supplementary material at <http://dx.doi.org/10.1116/1.4868027> for AFM data with measured heights as a function of helium ion doses; a plot of A.R. versus dose for Ne⁺; a summary of EDXS data; and experimental and simulated sputter yields.
- ⁵⁸M. A. Nguyen, M.-O. Ruault, and F. Fortuna, *Adv. Nat. Sci. Nanosci. Nanotechnol.* **3**, 015015 (2012).
- ⁵⁹H. R. Shanks and L. Ley, *J. Appl. Phys.* **52**, 811 (1981).
- ⁶⁰E. Oliviero, S. Peripolli, L. Amaral, P. F. P. Fichtner, M. F. Beaufort, J. F. Barbot, and S. E. Donnelly, *J. Appl. Phys.* **100**, 043505 (2006).
- ⁶¹W. B. A. Van Veen, T. R. Armstrong, K. T. Westerduin, L. M. Caspers, and J. Th.M. De Hosson, *Nucl. Instrum. Methods* **209/210**, 1055 (1983).